




Giant valley polarization and perpendicular magnetocrystalline anisotropy energy in monolayer MX_2 ($M = \text{Ru, Os}$; $X = \text{Cl, Br}$)

Weifeng Xie ¹, Long Zhang ¹, Yunliang Yue,² Min Li,¹ and Hui Wang ^{1,*}

¹*School of Physics, Hunan Key Laboratory of Super Microstructure and Ultrafast Process, Hunan Key Laboratory of Nanophotonics and Devices, State Key Laboratory of Powder Metallurgy, Central South University, Changsha 410083, China*

²*College of Information Engineering, Yangzhou University, Yangzhou 225127, China*



(Received 30 June 2023; revised 15 December 2023; accepted 18 December 2023; published 8 January 2024)

Large valley polarization and perpendicular magnetocrystalline anisotropy energy (PMAE) in room-temperature ferrovalley materials has been pursued for a long time because PMAE not only stabilizes long-range ferromagnetic (FM) order but also ensures spontaneous valley polarization. Herein, valley polarization and MAE of monolayer MX_2 ($M = \text{Ru, Os}$; $X = \text{Cl, Br}$) are investigated based on first-principles calculations, Wannier functions, and Monte Carlo simulations. It is found that OsBr_2 has a giant valley polarization of 327.158 meV and PMAE of 10.354 meV, ascribing to the strong spin-orbital coupling. The physical mechanism of valley polarization and PMAE are analyzed both qualitatively and quantitatively on the basis of perturbation theory, which shows that the valley polarization induces the distribution of MAE at K and K' valley points with opposite signs, and the couplings between d_{z^2} and d_{yz} , d_{xz} and d_{xy} , and $d_{x^2-y^2}$ and d_{yz} in opposite spin channels through orbital angular momentum operator \hat{L}_x have a dominant contribution to the total MAE. Moreover, doping of a few holes and biaxial compressive strain both remarkably improve the PMAE of OsBr_2 . Meanwhile, the compressive strain can enhance FM exchange coupling of OsBr_2 , increasing the Curie temperature T_c far beyond the room temperature. Additionally, doping of a few electrons can significantly increase the PMAE of room-temperature ferrovalley OsCl_2 to reach ~ 40 meV. In this paper, we elucidate the physical mechanism of the valley polarization and MAE and indicate that monolayer OsCl_2 and OsBr_2 are promising for application in valleytronic and magnetic storage devices at room-temperature condition.

DOI: [10.1103/PhysRevB.109.024406](https://doi.org/10.1103/PhysRevB.109.024406)

I. INTRODUCTION

Room-temperature ferromagnetic (FM) [1,2] and valley semiconductors [3–5] have received widespread attention. Ferrovalley materials which combine the charge and spin degrees of freedom with the valley degree of freedom have become a research hotspot in valleytronics, promising applications in encoding, manipulating, and transporting information [6,7]. The ferrovalley properties can be found in many two-dimensional FM materials akin to transition metal dichalcogenides due to the intrinsic absence of spatial inversion and time-reversal symmetry [4,8]. However, it is found that most of these ferrovalley materials have many disadvantages, such as small valley polarization in monolayer LaBr_2 [9]; small perpendicular magnetocrystalline anisotropy energy (PMAE) in monolayer GdCl_2 [10], FeClBr [11], RuCl_2 [12], FeCl_2 [13], and RuClX ($X = \text{F, Br}$) [14]; in-plane magnetic easy axis in monolayer GdI_2 [15] and FeClF [16]; or low Curie temperature in monolayer RuCl_2 [12] and FeCl_2 [17], which hinder their application in practical electronic devices. In recent years, searching for intrinsic two-dimensional ferrovalley materials with room-temperature FM semiconduction, large PMAE, and valley polarization has become the cutting edge in valleytronics.

Recently, the ferrovalley property of hexagonal monolayer MX_2 ($M = \text{Fe, Ru, Os}$; $X = \text{F, Cl, Br, I}$) has received much attention [11–13,16–25]. This family shows relatively ideal valley polarization and has an adjustable electronic property based on the value of Hubbard U , such as the U -driven half-valley metallicity and topological phase transition [16,18–20,22,25,26]. However, we noticed that the PMAE in some of these systems reaches >40 meV by means of adjusting U or strain [23]. However, the origin and regulation mechanism of the valley polarization and PMAE remains to be explored, particularly the relationship between the valley polarization and distribution of MAE in k space.

In this paper, we systemically investigate electronic, valley, and magnetic properties, uncovering the origin of valley polarization and PMAE in monolayer MX_2 ($M = \text{Ru, Os}$; $X = \text{Cl, Br}$). Based on the perturbation theory, it is found that the strong spin-orbital coupling (SOC) interaction takes major responsibility for the giant valley polarization and PMAE. Doping of a few electrons can significantly increase the PMAE of OsCl_2 , and doping of a few holes and biaxial compressive strain both remarkably improve the PMAE of OsBr_2 . The biaxial compressive strain can also greatly increase the FM exchange interaction and Curie temperature T_c of OsBr_2 . Second-order perturbation [27] and the torque method [28,29] are used for investigating the origin of the increment of PMAE, and the Heisenberg exchange parameter as a function of biaxial strain is calculated to explain the

*huiwang@csu.edu.cn

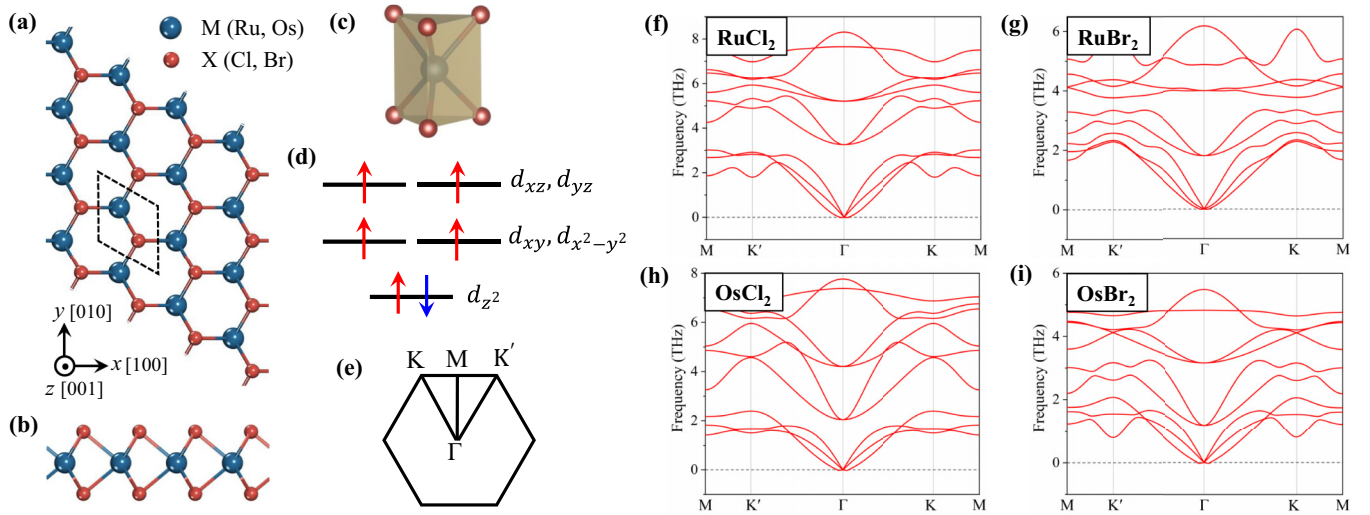


FIG. 1. Geometrical structure and phonon spectrum of monolayer MX_2 . (a) Top view and (b) side view of monolayer MX_2 , where the dashed box in (a) represents the unit cell, and the balls of dark blue and dark red label the M and X atoms, respectively. (c) Coordinate atom around M atom constituting the local structure of MX_6 . (d) Schematic illustration of energy level splitting of d orbitals caused by trigonal prism crystal field, the distribution of six d electrons of cation M in energy level shows a high-spin state. (e) First Brillouin zone (FBZ), where the high-symmetry points are marked. Phonon spectrums of monolayer (f) $RuCl_2$, (g) $RuBr_2$, (h) $OsCl_2$, and (i) $OsBr_2$.

variation of T_c . The above results indicate that monolayer $OsCl_2$ and $OsBr_2$ are promising candidates for application in valleytronic and magnetic storage devices at above room temperature.

II. CALCULATION DETAILS

First-principles calculations based on density functional theory are performed by using the projected augmented-wave method [30] implemented in VASP [31]. SOC parameters are included to calculate the electronic structures of valley polarization and the value of PMAE. The Perdew-Burke-Ernzerhof parameterization of the generalized gradient approximation is chosen as the exchange-correlation function [32]. The energy cutoff of the plane-wave basis is set as 500 eV for all monolayer MX_2 . Here, $U = 2$ eV is adopted to describe the strongly localized d orbitals of the M atom according to the available literature [12,21]. We also confirm the reasonability of $U = 2$ eV through comparing the band gap and spin-resolved band near the Fermi level between PBE+ U and HSE06, as shown in Figs. S1–S4 in the Supplemental Material [33]. A Γ -centered k -mesh grid of $12 \times 12 \times 1$ is used for the structural relaxation, electronic structure, and MAE calculation. The convergent threshold of energy is set as 1×10^{-6} eV, and that of the force is <0.01 eV \AA^{-1} . Based on the force theorem [34,35], MAE of MX_2 is calculated by the direct energy difference and torque methods [28,36,37] to obtain the energy difference between the x [100] and z [001] magnetization directions. The PHONOPY code [38] based on the finite displacement method is adopted to obtain the phonon dispersion spectrum of MX_2 by using a $6 \times 6 \times 1$ supercell. Berry curvature and anomalous valley Hall (AVH) conductivity are calculated by means of maximally localized Wannier functions as encoded in the WANNIER90 package [39]. Monte Carlo simulations with the Heisenberg model

[40,41] are performed to estimate T_c of monolayer $OsCl_2$ and $OsBr_2$.

III. RESULTS AND DISCUSSION

A. Structure and stability

The top and side views of monolayer MX_2 ($M = Ru, Os$; $X = Cl, Br$) are shown in Figs. 1(a) and 1(b); the geometrical structures are like monolayer MoS_2 in $2H$ phase, where the transition metal atoms are sandwiched by two anion layers. Figure 1(c) shows the local crystal structure around the M atom which forms a trigonal prism morphology with six X atoms. In a trigonal prism, the d orbitals of M can be split into e_1 ($d_{xy}, d_{x^2-y^2}$), e_2 (d_{xz}, d_{yz}), and a (d_{z^2}), in which a has the lowest energy, followed by e_1 and e_2 orbitals, as shown in Fig. 1(d). The six d electrons of cation M occupy these d orbitals with a high-spin state, forming a magnetic moment of $4 \mu_B$ in MX_2 . The first Brillouin zone (FBZ) is plotted in Fig. 1(e) where the high-symmetry points and paths are highlighted. In Figs. 1(f)–1(i), the phonon spectrums of MX_2 are obtained; the absence of imaginary frequencies in monolayer MX_2 indicates they are all dynamic stability.

The electronic structures of MX_2 without and with SOC are plotted in Fig. 2 ($RuCl_2$ and $RuBr_2$) and Fig. 3 ($OsCl_2$ and $OsBr_2$). It is shown that all MX_2 are FM half-semiconductors with a direct band gap and an out-of-plane magnetic easy axis; the energy differences between the FM and antiferromagnetic (AFM) states are shown in Table SI in the Supplemental Material [33]. As a comparison, it is found that the MAEs of $RuCl_2$ and $RuBr_2$ are far lower than that of $OsCl_2$ and $OsBr_2$. When the SOC is considered, an apparent valley polarization is presented when the magnetization is along the [001] direction, which means the MX_2 are all ferromagnetic materials [6]. The valley polarizations of monolayer $RuCl_2$, $RuBr_2$, and $OsBr_2$ have also been demonstrated in previous papers [12,20–23]. As we know, the large PMAE, valley polarization,

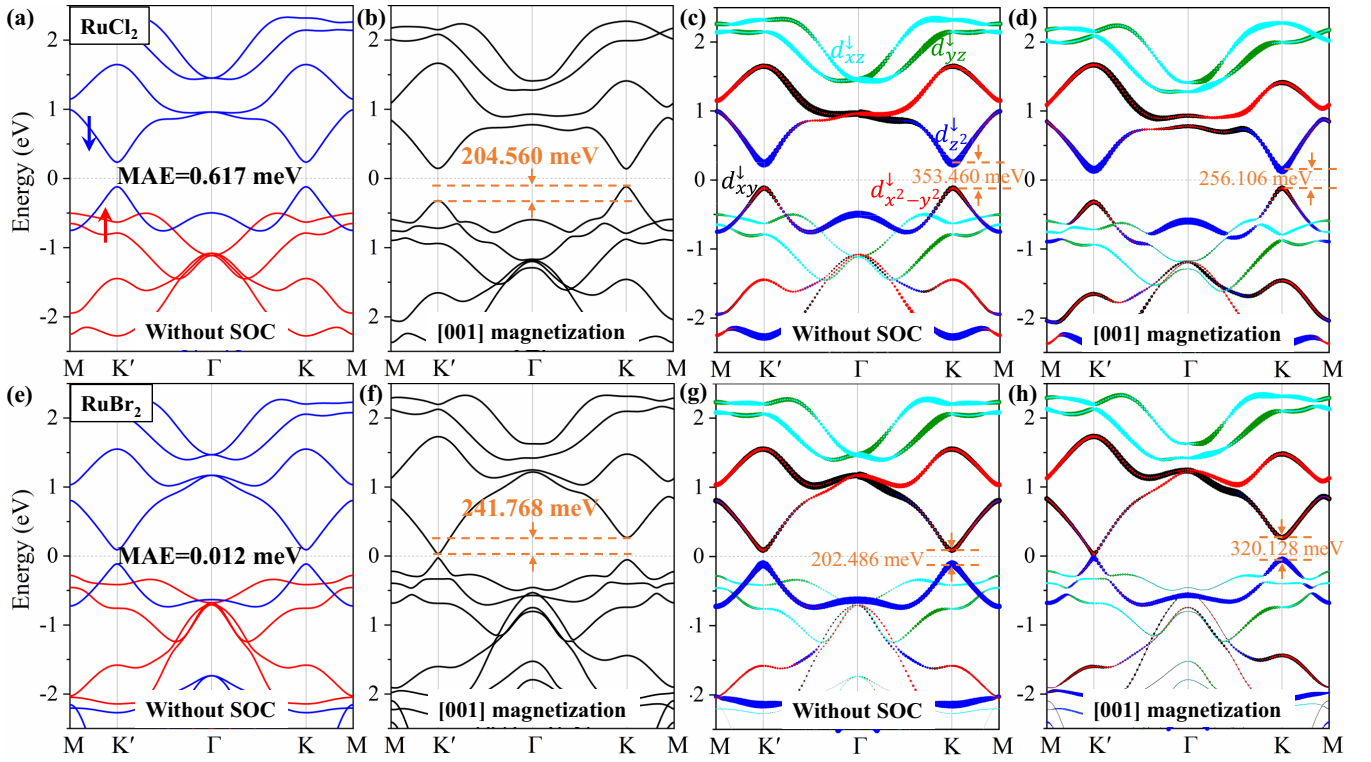


FIG. 2. Electronic structures and magnetocrystalline anisotropy energy (MAE) of monolayer RuCl_2 and RuBr_2 . Band structures (a) without considering spin-orbit coupling (SOC) and (b) with [001] magnetization in RuCl_2 . Bands (c) without considering SOC and (d) with [001] magnetization in RuCl_2 . (e)–(h) The same as (a)–(d) but for RuBr_2 . In (a), (b), (e), and (f), the MAE and valley polarization of the uppermost valence band (UVB) or lowermost conduction band (LCB) are marked, and the red and blue lines represent the spin-up and spin-down bands, respectively. In (c), (d), (g), and (h), the band gap at the K valley point is labeled. The Fermi level is set as zero on the band structures.

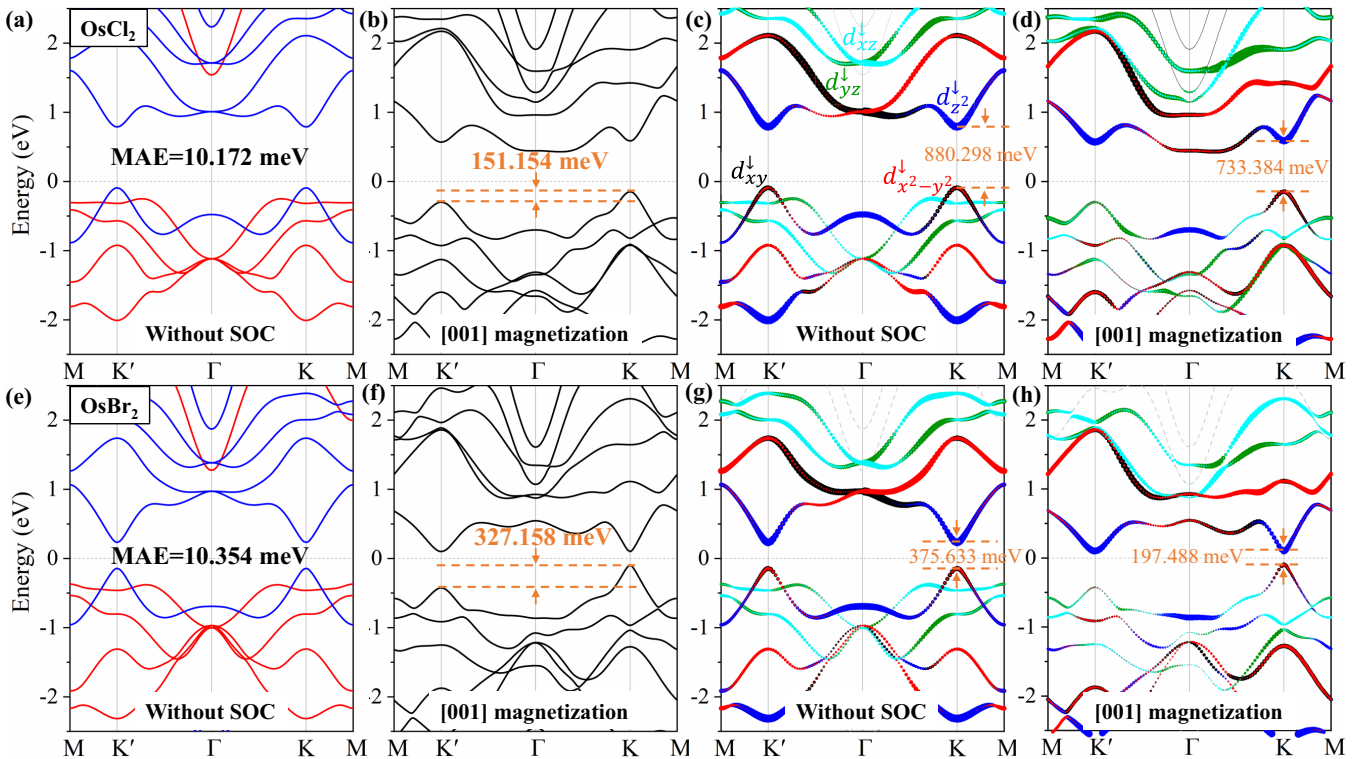


FIG. 3. Electronic structures and magnetocrystalline anisotropy energy (MAE) of monolayer OsCl_2 and OsBr_2 . (a)–(h) The same as Fig. 2 but for OsCl_2 and OsBr_2 .

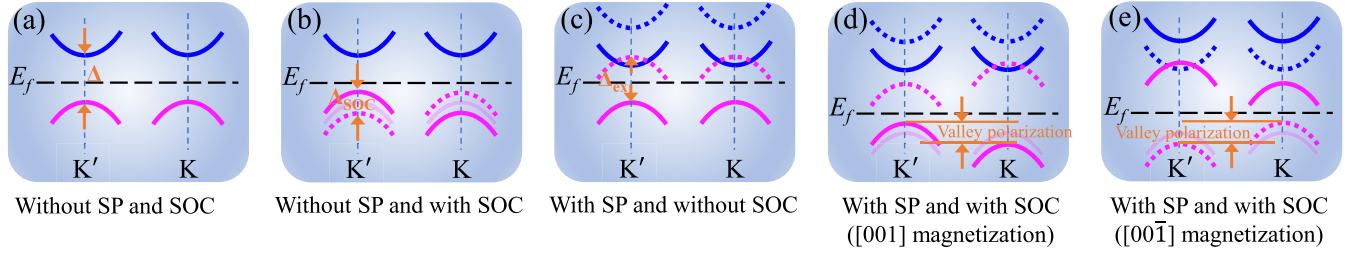


FIG. 4. Schematic illustration of the origin of valley polarization in ferrovalley materials. Band structures (a) without spin polarization (SP) and spin-orbit coupling (SOC), (b) without SP and with SOC, (c) with SP and without SOC, (d) with SP and with [001] magnetization, and (e) with SP and with [00 $\bar{1}$] magnetization, where solid and dashed lines represent spin-up and spin-down bands, respectively, translucent pink lines are used as eyes to mark the bands without SOC perturbation, pink represents the hybridization bands contributed by d_{xy} and $d_{x^2-y^2}$, and blue represents the bands contributed by d_{z^2} . E_f represents the Fermi level.

and high Curie temperature in ferrovalley materials have been pursued for a long time in practical application. In Figs. 3(a), 3(b), 3(e), and 3(f), it is found that large PMAE (~ 10 meV) and valley polarization (> 150 meV) are presented in OsCl₂ and OsBr₂; the PMAE is highlighted compared with the most intrinsic two-dimensional magnetic materials, such as monolayer CrI₃ [42], Fe₃GeTe₂ [43], and CrTe₂ [44]. Especially for monolayer OsBr₂, the SOC with [001] magnetization induces a giant valley polarization at K and K' high-symmetry points. It is surprisingly that the large PMAE of 10.354 meV and remarkable valley polarization of 327.158 meV coexist in OsBr₂, which benefits its application both in magnetic storage and valleytronics.

B. Ferrovalley of monolayer MX_2

Usually, the total Hamiltonian of ferrovalley materials can be constructed as [6]

$$\hat{\mathcal{H}}(k) = \hat{\mathcal{H}}_0(k) + \hat{\mathcal{H}}_{\text{SOC}}(k) + \hat{\mathcal{H}}_{\text{ex}}(k), \quad (1)$$

where $\hat{\mathcal{H}}_{\text{SOC}}$ and $\hat{\mathcal{H}}_{\text{ex}}$ are the SOC term and intrinsic magnetic exchange interaction terms, respectively. The SOC and exchange interaction are the main origins of the formation of spontaneous valley polarization in ferrovalleys. From Figs. 4(a) and 4(b), one can see that the SOC lifts the degeneracy of spin-up and spin-down states and induces the valley-related SOC splitting (Δ_{SOC}) at both K and K' valley points. However, due to the time-reversal symmetry, it is still degenerate at two valley points and has an absence of valley polarization, like the monolayer MoS₂ family [45]. Therefore, an effective external stimulus needs to be applied to break the time-reversal symmetry and lift the valley degeneracy energetically in the MoS₂ family, such as an external magnetic field [46,47]. For ferrovalley materials, an intrinsic FM exchange interaction causes a separation of spin-up and spin-down bands and forms an exchange splitting (Δ_{ex}), shown in Fig. 4(c). When considering both SOC and the exchange interaction with [001] magnetization, the exchange interaction can lift valley degeneracy at K and K' valley points and induce the valley polarization; however, the magnitude of spin splitting induced by SOC will not be impacted by the exchange interaction, as shown in Fig. 4(d). Similarly, when the magnetization is reversed, the valley polarization is also

formed, but the direction is opposite at K and K' valley points, shown in Fig. 4(e).

Take monolayer OsBr₂ as an example. We concretely investigate the physical origin of the large valley polarization. The d -orbital-resolved band structure of Os is plotted in Fig. 3(g). It is found that the valence band maximum (VBM) and conduction band minimum (CBM) are essentially contributed by d_{xy}^{\downarrow} ($d_{x^2-y^2}^{\downarrow}$) and $d_{z^2}^{\downarrow}$, respectively, at K and K' valley points. Only the SOC Hamiltonian of the spin-conserving term needs to be considered and can be written as [48]

$$\hat{\mathcal{H}}_{\text{SOC}} = \lambda \hat{S}_z (\hat{L}_z \cos\theta + \frac{1}{2} \hat{L}_+ e^{-i\varphi} \sin\theta + \frac{1}{2} \hat{L}_- e^{i\varphi} \sin\theta), \quad (2)$$

where λ represents the SOC coefficient, and θ and φ represent the polar and azimuth angles, respectively, labeled in Fig. S5 in the Supplemental Material [33]. We only consider the variation of θ in the xz plane. Then $\varphi = 0$. Equation (2) can be deduced to

$$\hat{\mathcal{H}}_{\text{SOC}} = \lambda \hat{S}_z (\hat{L}_z \cos\theta + \hat{L}_x \sin\theta). \quad (3)$$

Then only considering the impact of the SOC term on band energy at K or K' valley points, corresponding to Fig. 4(b), the coupling matrix representation among $d_{x^2-y^2}^{\downarrow}$, d_{xy}^{\downarrow} , and $d_{z^2}^{\downarrow}$ through the spin-conserving SOC Hamiltonian [Eq. (3)] can be constructed, written as

$$[\mathcal{H}] = [\mathcal{H}_0] + [\mathcal{H}_{\text{SOC}}] = \begin{bmatrix} \varepsilon_0 & -i\lambda \cos\theta & 0 \\ i\lambda \cos\theta & \varepsilon_0 & 0 \\ 0 & 0 & \varepsilon_0 + \Delta \end{bmatrix}, \quad (4)$$

where we treat \hat{S}_z in Eq. (3) as $\frac{1}{2}$, ε_0 and $\varepsilon_0 + \Delta$ represent the VBM and CBM energy levels without SOC perturbation at the K or K' valley point, respectively, and Δ is the band gap between VBM and CBM. Through diagonalizing the matrix in Eq. (4), three eigenvalues corresponding to the energy levels after perturbation are obtained as follows:

$$\varepsilon_1 = \varepsilon_0 + \Delta, \quad (5)$$

$$\varepsilon_2 = \varepsilon_0 + \lambda \cos\theta, \quad (6)$$

$$\varepsilon_3 = \varepsilon_0 - \lambda \cos\theta. \quad (7)$$

In ferrovalley materials, combining the exchange interaction, ε_1 , ε_2 , and ε_3 correspond to the energy level of CBM, uppermost valence band (UVB) at the K valley point, and

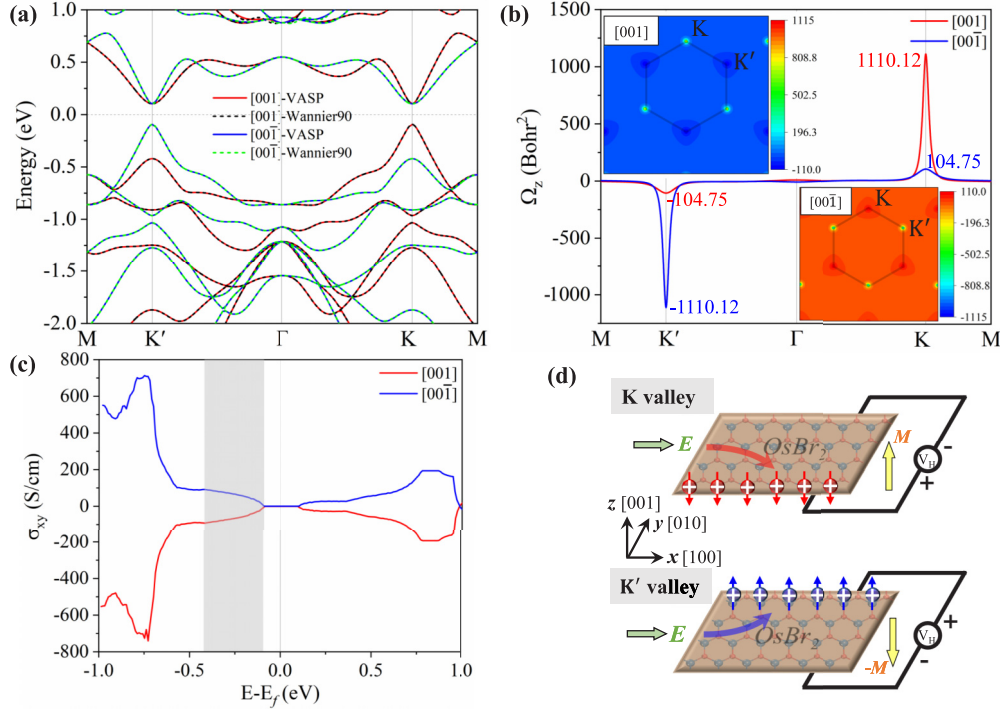


FIG. 5. Anomalous valley Hall (AVH) effect of monolayer OsBr₂. (a) A comparison of band structure calculated based on the VASP and WANNIER90 packages. (b) Distribution of Berry curvature along the high-symmetry path when the magnetization is along [001] and [00 $\bar{1}$] directions; the insets show the distribution of Berry curvatures in the first Brillouin zone (FBZ). (c) AVH conductivity with [001] and [00 $\bar{1}$] magnetization directions. (d) Schematic illustrations of AVH effect at K and K' valley points.

UVB at the K' valley point, respectively, after perturbation, shown in Fig. 4(d) or 4(e).

Additionally, considering the C_{3h} crystalline symmetry of MX_2 and combining the transition of spherical harmonics of d orbitals, one can also derive the valley polarization of the VBM (CBM) (as shown in Sec. V in the Supplemental Material [33]) based on two-band perturbation model, which can be written as

$$\begin{aligned} \Delta E_{c(v)} &= E_{c(v)}^{+1} - E_{c(v)}^{-1} = \langle \varphi_{c(v)}^{+1} | \hat{\mathcal{H}}_{\text{SOC}} | \varphi_{c(v)}^{+1} \rangle \\ &\quad - \langle \varphi_{c(v)}^{-1} | \hat{\mathcal{H}}_{\text{SOC}} | \varphi_{c(v)}^{-1} \rangle = 0, \end{aligned} \quad (8)$$

$$\begin{aligned} \Delta E_{v(c)} &= E_{v(c)}^{+1} - E_{v(c)}^{-1} = \langle Y_2^{+2} | \hat{\mathcal{H}}_{\text{SOC}} | Y_2^{+2} \rangle \\ &\quad - \langle Y_2^{-2} | \hat{\mathcal{H}}_{\text{SOC}} | Y_2^{-2} \rangle = 2\lambda \cos\theta. \end{aligned} \quad (9)$$

Noteworthy, for OsBr₂, in Fig. S6(d) in the Supplemental Material [33], the projected band along the z -axis component of the spin is plotted. It is found that a band inversion occurs at the K' valley point, which is anomalous as compared with the K valley point. The apparent variation of d orbitals at the K' valley point between the d -orbital-resolved bands without SOC perturbation and that with [001] magnetization also illustrates the band inversion at the K' valley point, as shown in Figs. 3(g) and 3(h). Therefore, the SOC coefficient λ in OsBr₂ is obtained according to the SOC perturbation at the K valley point. In Fig. 3(g), without SOC perturbation, the band gap at the K valley point is $\Delta = 375.633$ meV. When the magnetization is along the [001] direction, corresponding to $\theta = 0^\circ$, the band gap decreases to $\varepsilon_1 - \varepsilon_2 = 197.488$ meV.

Combining Eqs. (5) and (6), the SOC coefficient λ in OsBr₂ can be calculated as 178.145 meV, which is three times larger than Gd adsorbed on a graphene nanoribbon [49] and comparable with monolayer WX₂ ($X = \text{S, Se, Te}$) [50]. Such large SOC is the major reason for giant valley polarization in monolayer OsBr₂.

For monolayer OsCl₂, the phenomenon is the same as that of OsBr₂: $d_{x^2-y^2}^\downarrow$, d_{xy}^\downarrow , and $d_{z^2}^\downarrow$ orbitals contribute the VBM and CBM, respectively, at K and K' valley points, as shown in Fig. 3(c). From Fig. 3(d), we find that the band gap at the K point changes from 880.298 to 733.384 meV after the SOC is considered. According to Eqs. (5) and (6), the SOC coefficient λ in OsCl₂ is 146.914 meV. Similarly, for RuCl₂ and RuBr₂, as shown in Figs. 2(c), 2(d), 2(g), and 2(h), the calculated SOC coefficients are 97.354 and 117.642 meV, respectively. Substituting the SOC coefficient λ into Eq. (9), we obtain the valley polarizations of RuCl₂ and RuBr₂, which are 194.708 and 235.284 meV, respectively. These results are approximately consistent with the acquired values from the first-principles calculations.

FM materials with valley polarization are also named ferrovalley materials [6], which are useful in information storage, transmission, and encoding. Next, we demonstrate the AVH effect in the ferrovalley of OsBr₂ based on the Berry curvatures and AVH conductivity. The band structures of [001] and [00 $\bar{1}$] magnetizations near the Fermi level based on Wannier functions are plotted in Fig. 5(a), guaranteeing the accuracy of the calculated Berry curvatures and AVH conductivity. Based on the Kubo formula [51], the Berry curvatures $\Omega_z(k)$ along

the [001] and [00 $\bar{1}$] magnetizations can be written as

$$\Omega_z(k) = - \sum_n \sum_{n \neq m} f_n(\mathbf{k}) \frac{2\text{Im} \langle \psi_{n\mathbf{k}} | \hat{v}_x | \psi_{m\mathbf{k}} \rangle \langle \psi_{m\mathbf{k}} | \hat{v}_y | \psi_{n\mathbf{k}} \rangle}{(E_{n\mathbf{k}} - E_{m\mathbf{k}})^2}, \quad (10)$$

where $f_n(\mathbf{k})$ and $\hat{v}_{x(y)}$ are the Fermi-Dirac distribution function and the x (y) component of the velocity operator, respectively, and $E_{n(m)\mathbf{k}}$ is the eigenvalue of Bloch wave function $\psi_{n(m)\mathbf{k}}$. The Berry curvatures are plotted in Fig. 5(b) under [001] and [00 $\bar{1}$] magnetizations. As can be seen, there are considerable Berry curvatures with opposite signs and different magnitudes at K and K' valley points when the magnetization is along the [001] direction. In contrast, as the magnetization direction is reversed to the [00 $\bar{1}$] direction, the magnitudes of Berry curvature at the K and K' valley points are interconverted with opposite signs. Obviously, the different absolute values of Berry curvature with opposite signs at K and K' valley points verify the valley-contrasting characteristic of monolayer OsBr₂.

The AVH conductivity σ_{xy} is obtained by integrating the Berry curvature of Eq. (10) over the Brillouin zone according to the following formula:

$$\sigma_{xy} = - \frac{e^2}{\hbar} \int_{\text{BZ}} \frac{d\mathbf{k}}{(2\pi)^2} \Omega_z(\mathbf{k}). \quad (11)$$

The valley polarization exists in UVB, corresponding to the shadow area of Fig. 5(c). One may note that proper hole

doping is desired to shift the Fermi level for transport applications. The existence of nonzero perpendicular Berry curvature can be viewed as an effective magnetic field; if an external electric field along the x -axis [100] direction is imposed, the Bloch holes will be provoked by an electric field and effective magnetic field and then produce an anomalous y -axis [010] velocity $\mathbf{v}_y \sim \mathbf{E}_x \times \Omega_z(\mathbf{k})$. Finally, the spin-polarized holes under the [001] ([00 $\bar{1}$]) magnetizations are accumulated at one of the edges at the K (K') valley point, and the AVH voltage could further be generated, as schematically illustrated in Fig. 5(d). In Fig. S7 in the Supplemental Material [33], the Berry curvatures and AVH conductivity of RuCl₂, RuBr₂, and OsCl₂ are also plotted. It is concluded that all monolayer MX_2 have a spontaneous valley-polarization-induced AVH effect, which can be used in valleytronics.

C. The origin of PMAE

A strong PMAE is preferred in magnetic storage devices to enhance the stability against the external noises induced by thermal fluctuation, magnetic field, and electric current but also is the prerequisite of spontaneous valley polarization. Thus, it is necessary to explore the origin and manipulation of MAE in ferrovalley MX_2 .

The MAE is statistically originated from coupling between key pairs of electronic states near the Fermi level, as reflected by the variation of band structure in the FBZ induced by rotating magnetization from magnetic hard axis to easy axis, written as [49]

$$\text{MAE} = E_{[100]} - E_{[001]} = \sum_{k \in \text{FBZ}} \left\{ \sum_{i \in \text{BANDS}} [\varepsilon_i^{[100]}(k) f_i^{[100]}(k) - \varepsilon_i^{[001]}(k) f_i^{[001]}(k)] w(k) \right\}, \quad (12)$$

where $\varepsilon(k)$, $f(k)$, and $w(k)$ are the band energy, the filling factor, and the weight at a point k in the FBZ, respectively, and the subscript i stands for the i th band; i contains all bands. The distribution of MAE in the k space of FBZ is shown in Figs. 6(a)–6(d). It is found that the sign of MAE at K and K' valley points is opposite with negative MAE near K and positive MAE near K' for RuCl₂, OsCl₂, and OsBr₂; however, the phenomenon is opposite for RuBr₂ due to the distinct valley polarization located on the lowermost conduction band (LCB). The MAE is almost zero at the other k space, which means that the distributions of MAE near K and K' have a dominant contribution to the total MAE.

This distribution of MAE in k space can be explained by Eqs. (5)–(7) and (12). Equations (5)–(7) show the energy level of the CBM after perturbation is almost unchanged, and the energy levels of the VBM at the K and K' valley points are upward and downward shifted, respectively, for RuCl₂, OsCl₂, and OsBr₂. Additionally, it is easily obtained that the [100] magnetization ($\theta = 90^\circ$) will not shift the energy levels of the VBM and CBM according to Eqs. (5)–(7). Combining Eq. (12) and setting k as the k point around K and K' valley points, it can be concluded that the sign of MAE around the K and K' valley points is opposite in most valley materials.

Essentially, SOC is an important reason for MAE, as demonstrated from the second-order perturbation [27]. In RuCl₂ and RuBr₂, it is found that the contribution to the MAE from the coupling of d orbitals of Ru only occupies 78.11 and 13.89%, respectively, and a large part of the contribution of MAE comes from p orbitals of Ru and Cl or Br, which is like the phenomenon of monolayer $2H\text{-FeBr}_2$ [18]. The distributed chart is shown in Figs. S8(a) and S8(b) in the Supplemental Material [33]. In Figs. 6(e) and 6(f), we find that the transition between $d_{x^2-y^2}$ and d_{xy} , d_{xz} and d_{yz} contributes to a negative MAE, and the transitions between d_{z^2} and d_{yz} , d_{xz} and d_{xy} , and $d_{x^2-y^2}$ and d_{yz} have a major positive contribution to total MAE. In Figs. S8(e)–S8(h) in the Supplemental Material [33], the positive MAE is mainly contributed by the transitions between p_x and p_y of Ru and Cl or Br.

In OsCl₂ and OsBr₂, it is found that the contribution to the MAE from the coupling of Os- d orbitals occupies 95.11 and 92.50%, respectively, which significantly differs from RuCl₂ and RuBr₂, as shown in Figs. S8(c) and S8(d) in the Supplemental Material [33]. Take OsBr₂ as an example. Based on second-order perturbation, we qualitatively discuss the contribution of MAE according to the coupling matrix and projected density of states (PDOS) of Os- d orbitals, as shown in Figs. 6(h) and 7(c), respectively. It is found that

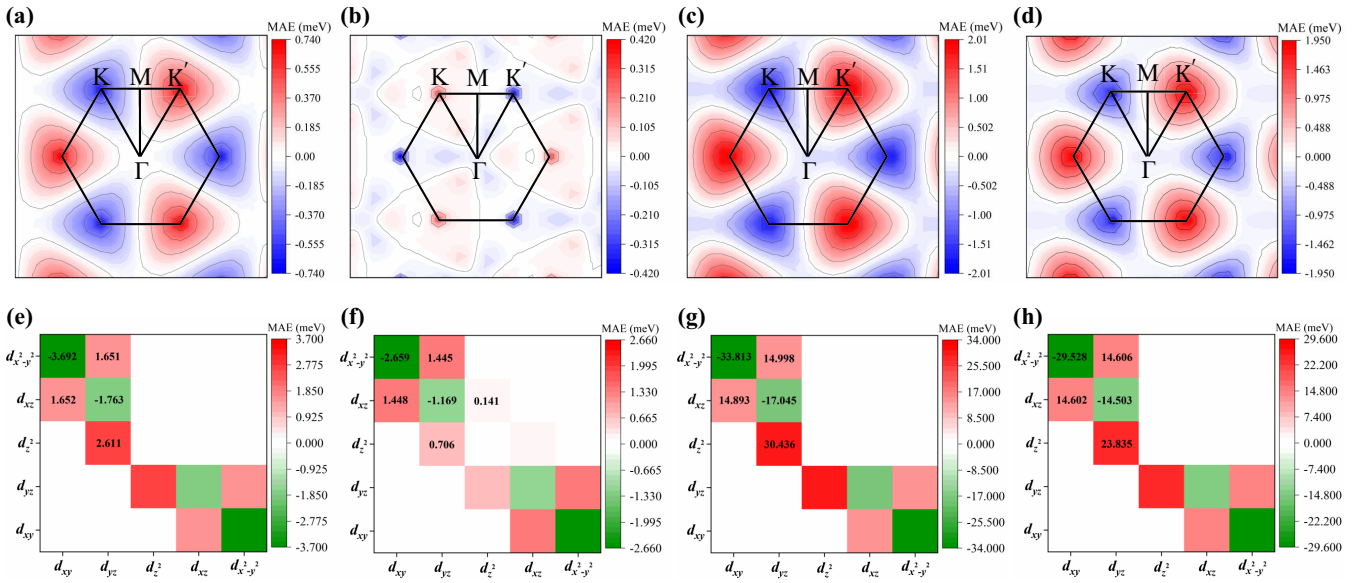


FIG. 6. Origin of perpendicular magnetocrystalline anisotropy energy (PMAE) in monolayer MX_2 . Distribution of MAE in the first Brillouin zone (FBZ) for (a) RuCl₂, (b) RuBr₂, (c) OsCl₂, and (d) OsBr₂. Contribution of transition between different d orbitals of Ru in (e) RuCl₂ and (f) RuBr₂, Os in (g) OsCl₂ and (h) OsBr₂ to MAE.

the transition between $d_{x^2-y^2}$ and d_{xy} contributes to a negative MAE of -29.528 meV, and a negative contribution of -14.503 meV to the MAE is induced by the transition be-

tween d_{xz} and d_{yz} . In contrast, the transitions between d_z^2 and d_{yz} , d_{xz} and d_{xy} , and $d_{x^2-y^2}$ and d_{yz} have positive contributions of 23.835, 14.602, and 14.606 meV, respectively. It

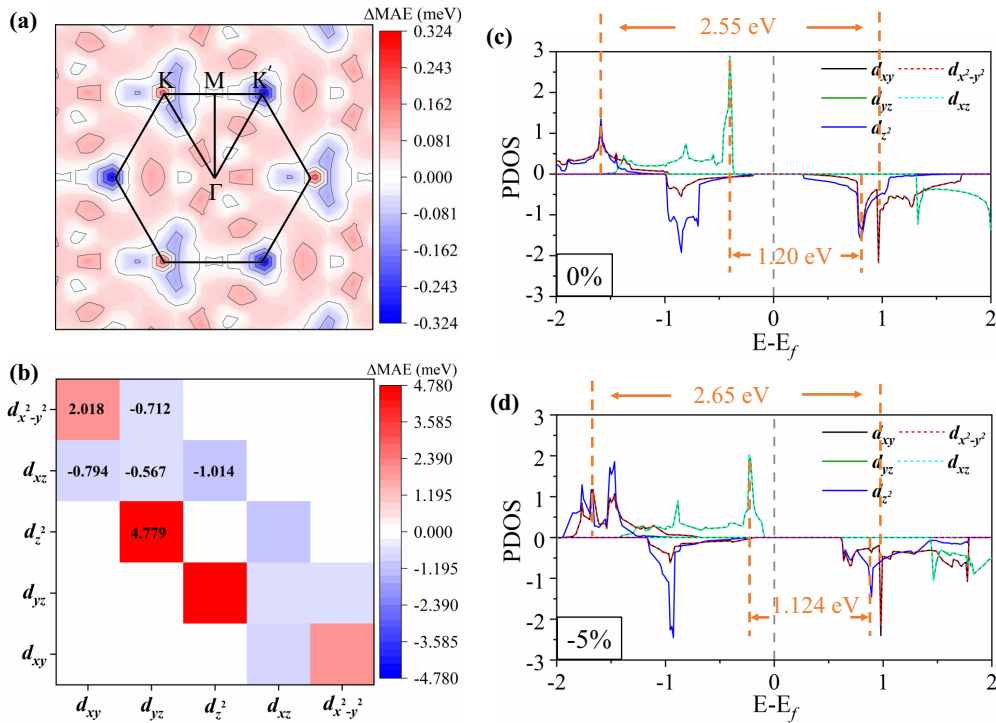


FIG. 7. For OsBr₂, (a) distribution of energy difference of magnetocrystalline anisotropy energy (MAE) between 0% strain and -5% compressive strain in the first Brillouin zone (FBZ). (b) Variation of MAE contributed by the transition between different Os- d orbitals. (c) Projected density of states (PDOS) of Os- d orbitals, where some energy intervals of different d orbitals are labeled. (d) Same as (c) but for -5% compressive strain.

TABLE I. The coupling matrix elements between different d orbitals through orbital angular momentum operator \hat{L}_z and \hat{L}_x .

$ u\rangle$	\hat{L}_z					\hat{L}_x				
	d_{xy}	d_{yz}	d_{z^2}	d_{xz}	$d_{x^2-y^2}$	d_{xy}	d_{yz}	d_{z^2}	d_{xz}	$d_{x^2-y^2}$
d_{xy}	0	0	0	0	$2i$	0	0	0	$-i$	0
d_{yz}	0	0	0	i	0	0	0	$-\sqrt{3}i$	0	$-i$
d_{z^2}	0	0	0	0	0	0	$\sqrt{3}i$	0	0	0
d_{xz}	0	$-i$	0	0	0	i	0	0	0	0
$d_{x^2-y^2}$	$-2i$	0	0	0	0	0	i	0	0	0

is known that the second-order perturbation can be written as [27]

$$\Delta E_{\pm,\pm} = \lambda^2 \sum_{o,u} \frac{|\langle o^\pm | \hat{L}_z | u^\pm \rangle|^2 - |\langle o^\pm | \hat{L}_x | u^\pm \rangle|^2}{\varepsilon_u^\pm - \varepsilon_o^\pm}, \quad (13)$$

$$\Delta E_{\pm,\mp} = -\lambda^2 \sum_{o,u} \frac{|\langle o^\pm | \hat{L}_z | u^\mp \rangle|^2 - |\langle o^\pm | \hat{L}_x | u^\mp \rangle|^2}{\varepsilon_u^\pm - \varepsilon_o^\mp}. \quad (14)$$

Equations (13) and (14) correspond to the contribution of the same spin channel and different spin channel to the MAE, respectively. Here, λ is the SOC coefficient, and the corner marks o , u , $+$, and $-$ represent the occupied, unoccupied, spin-up, and spin-down channels, respectively. Only the coupling of Os- d orbitals through the orbital angular momentum operator (\hat{L}_z and \hat{L}_x) needs to be considered, as listed in Table I.

As can be seen from Table I,

$$\langle d_{x^2-y^2} | \hat{L}_z | d_{xy} \rangle = -2i. \quad (15)$$

Combining with the PDOS shown in Fig. 7(c), it is found that $d_{x^2-y^2}$ and d_{xy} orbitals are degenerate, which mainly distributes in occupied spin-up and unoccupied spin-down channels. Substituting Eq. (15) into Eq. (14), we obtain

$$\Delta E_{+,-} = -\lambda^2 \sum_{o,u} \frac{4}{\varepsilon_u^- - \varepsilon_o^+}, \quad (16)$$

which contributes a dominant negative MAE. Equation (16) further verifies the negative MAE contributed by the transition between $d_{x^2-y^2}$ and d_{xy} shown in Fig. 6(h). Similarly, from Table I,

$$\langle d_{xz} | \hat{L}_z | d_{yz} \rangle = -i, \quad (17)$$

and d_{xz} and d_{yz} orbitals are degenerate. They are distributed in both occupied spin-up and unoccupied spin-down channels. Substituting Eq. (17) into Eq. (14), we can obtain

$$\Delta E_{+,-} = -\lambda^2 \sum_{o,u} \frac{1}{\varepsilon_u^- - \varepsilon_o^+}, \quad (18)$$

which has a negative contribution to the MAE.

Next, Fig. 6(h) shows the positive contributions to the MAE originate from the transition between d_{z^2} and d_{yz} , d_{xz} and d_{xy} , and $d_{x^2-y^2}$ and d_{yz} . In Fig. 7(c), we find that d_{z^2} orbitals distribute not only in the occupied spin-up and spin-down channels but also in the unoccupied spin-down channels. Con-

sidering the coupling matrix elements of d orbitals in Table I, we only need to focus on the following coupling elements:

$$\langle d_{yz}^+ | \hat{L}_x | d_{z^2}^- \rangle = -\sqrt{3}i, \quad (19)$$

$$\langle d_{xz}^+ | \hat{L}_x | d_{xy}^- \rangle = i, \quad (20)$$

$$\langle d_{yz}^+ | \hat{L}_x | d_{x^2-y^2}^- \rangle = -i. \quad (21)$$

Substituting Eqs. (19)–(21) into Eq. (14), positive MAE can be obtained. The energy difference ($\varepsilon_{d_{z^2}}^- - \varepsilon_{d_{yz}}^+$) between d_{yz}^+ and $d_{z^2}^-$ has the lowest value, which renders the largest positive MAE, as shown in Fig. 6(h).

The torque method is a useful tool to analyze the contribution of MAE [36,37], which can quantitatively resolve the contribution between the same or different spin channels to the total MAE. The calculated results show that the couplings between spin-up and spin-up (1.514 meV) as well as that between spin-down and spin-down (1.300 meV) are very small, while most contributions to MAE stem from the coupling between spin-up and spin-down channels (7.717 meV), as shown in Fig. 8(d). Furthermore, we can see that the PMAE in OsBr₂ is very robust against electron or hole doping, which is also beneficial to the application of monolayer OsBr₂ in valleytronics due to the indispensable hole doping.

D. Carrier doping and biaxial strain regulation

The calculated MAEs of RuCl₂, RuBr₂, and OsCl₂ by the torque method are also shown in Figs. 8(a)–8(c). The calculated values agree well with the energy difference method. Apparently, doping of a few carriers cannot vary the direction of MAE. Especially for OsCl₂, electron doping can significantly increase the PMAE, reaching ~40 meV, and hole doping can also increase the MAE for OsCl₂ and OsBr₂. To explore the impact of carrier doping on the MAE and valley polarization, in Fig. S9 in the Supplemental Material [33], we show the variation of MAE with the carrier doping based on the energy difference method in OsCl₂. The variation trends on a small scale are consistent with the torque method. In OsCl₂, a 0.2 electron doping induces the MAE to reach 37.62 meV. In OsBr₂, we emphatically investigate the influence of hole doping on the shift of the Fermi level due to the application of the prominent AVH effect, as shown in Fig. S10 in the Supplemental Material [33]. It is found that the hole doping from 0.01 to 0.11 can render the Fermi level shift to between two valley points. At this point, the PMAE increases monotonously with the hole doping and reaches 22.03 meV at 0.11 hole doping, shown in Fig. 9(a). However, the valley polarization of UVB is decreased, but the value is always >250 meV. In short, we demonstrate the hole doping is a feasible approach to improve the application of OsBr₂ in valleytronics.

As a suitable substrate is indispensable to the growth of two-dimensional materials, the impact of inevitable biaxial strain on the valley polarization and PMAE is important for practical application. Additionally, strain and the change of Hubbard U have the same effect on the regulation of electronic properties for MX_2 [22]. Due to the uncertainty of accurate U , we investigate the impact of biaxial strain on the valley

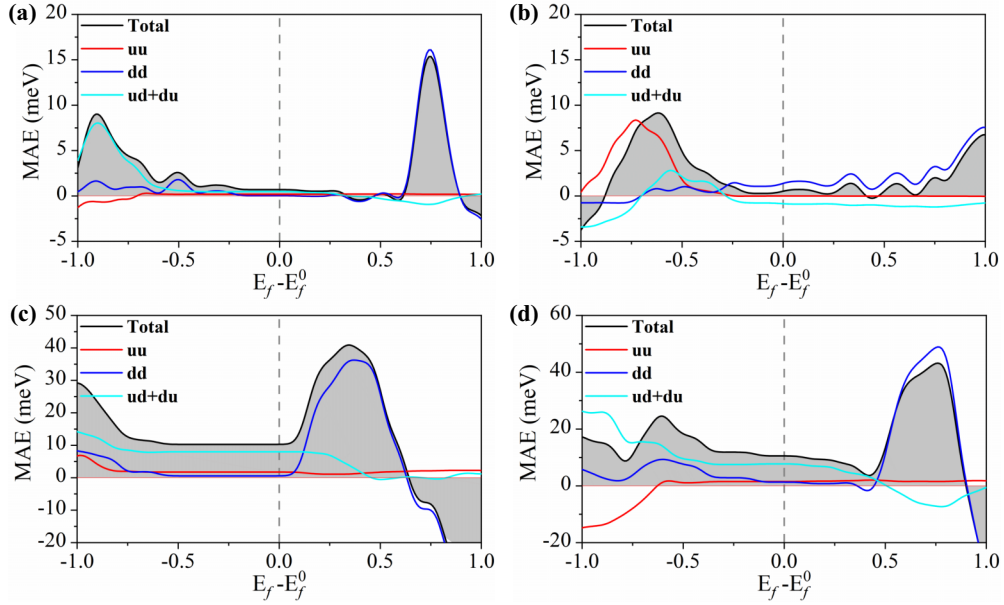


FIG. 8. Quantitative contribution of the same spin channel (uu or dd) and opposite spin channel (ud + du) to magnetocrystalline anisotropy energy (MAE) in (a) RuCl₂, (b) RuBr₂, (c) OsCl₂, and (d) OsBr₂ based on torque method, where E_f^0 stands for the natural Fermi level of the system.

polarization and PMAE. Take monolayer OsBr₂ as an example. Figure 9(b) shows the PMAE and valley polarization of UVB or LCB as a function of biaxial strain. It is found that tensile strain of 2 and 5% increase the valley polarization of UVB and LCB to ~ 400 and 372 meV, respectively. However, PMAE decreases almost monotonously from compressive to tensile strain. It is noticed that the PMAE reaches 14.316

meV at compressive strain -5% . The strain-induced increased MAE inspires us to exploit the reasons for variation compared with the intrinsic state.

In Fig. 7(a), the difference of MAE in k space of the FBZ between -5 and 0% strain is plotted. It is found that the increments of MAE near the K and Γ points contribute to the increment of total PMAE. We also analyze the difference of

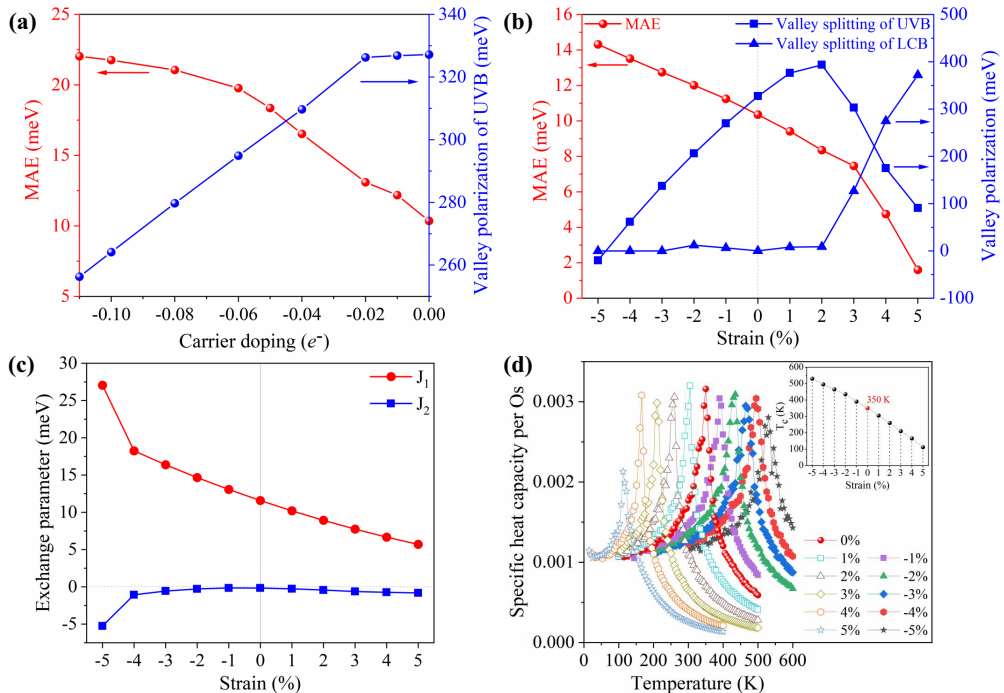


FIG. 9. For OsBr₂, the variation of magnetocrystalline anisotropy energy (MAE) and valley polarization as a function of (a) carrier doping and (b) biaxial strain. (c) Nearest-neighbor exchange parameter J_1 and next-nearest-neighbor exchange parameter J_2 vs strain. (d) Specific heat capacity per Os as a function of temperature under different strains; the inset shows the Curie temperature T_c vs strain.

coupling matrix elements of d orbitals between -5 and 0% strains, shown in Fig. 7(b). It is found that the transitions between d_{z^2} and d_{yz} , $d_{x^2-y^2}$ and d_{xy} have a dominant increased MAE, which can be confirmed by comparing the shifting of energy levels of d orbitals in PDOS between -5 and 0% strain according to the second-order perturbation in Eqs. (13) and (14). The increased total MAE mainly ascribes to the diminished energy interval between $d_{z^2}^-$ and d_{yz}^+ and enlarged energy interval between $d_{x^2-y^2}^-$ and d_{xy}^+ , as shown in Figs. 7(c) and 7(d). In Fig. S11 in the Supplemental Material [33], the torque method shows that the contribution from the coupling between spin-up and spin-up, spin-down and spin-down, and opposite spin channels are 0.621, 3.904, and 9.916 meV, respectively. The apparent increased coupling between opposite spin channels verifies the variation of MAE in terms of the analysis of second-order perturbation.

The magnetic exchange parameters of OsCl₂ and OsBr₂ are calculated based on the Heisenberg model:

$$\mathcal{H} = -\frac{1}{2} \sum_{(ij)} J_{ij} S_i^z S_j^z - A \sum_i (S_i^z)^2, \quad (22)$$

where J_{ij} represents the exchange strength between the magnetic atoms at i and j sites, S is the spin of the magnetic atom, the superscript z represent the z component of the spin, and A is the value of MAE. The nearest-neighbor exchange J_1 and next-nearest-neighbor exchange J_2 are considered in a $4 \times 4 \times 1$ supercell, as shown in Sec. X in the Supplemental Material [33]. The simulated results show that Curie temperature T_c from the FM to the paramagnetic state is ~ 350 K in OsBr₂ and 495 K in OsCl₂, far higher than room temperature, as shown in the inset of Figs. 9(d) and S13 in the Supplemental Material [33], respectively. To see how strain affects T_c , we further investigate the strain-dependent J_1 and J_2 in OsBr₂, as shown in Fig. 9(c). It is found that J_1 and J_2 decrease with the tensile strain, and J_1 is enhanced significantly to 27.05 meV, while J_2 has a negative value and decreases remarkably down to -5.24 meV at -5% compressive strain since J_1 is far larger than that of J_2 , indicating that the FM ground state is always remained robustly. As T_c is closely related to J_1 , J_2 , and MAE, the strain-dependent T_c is plotted in the inset of Fig. 9(d). As can be seen, T_c increases almost linearly from tensile to compressive strain. Specifically,

-5% compressive strain increases T_c to 530 K. Therefore, large tunability of T_c by strain engineering is beneficial for the application of monolayer OsBr₂ under high-temperature conditions.

IV. CONCLUSIONS

In summary, based on first-principles calculations, Wannier functions, Monte Carlo simulation, and perturbation theory, we systematically investigate the valley polarization and PMAE of monolayer MX_2 and elucidate their origins. It is shown that monolayer OsBr₂ has a giant valley polarization and PMAE, reaching 327.158 and 10.354 meV, respectively. It is found that the strong SOC is responsible for the giant valley polarization and PMAE, the valley polarization induces the distribution of MAE at K and K' valley points with opposite signs, and the coupling of electronic states in opposite spin channels of Os- d orbitals has a major contribution to the MAE. Moreover, doping of a few holes and biaxial compressive strain both remarkably improve the PMAE, and the compressive strain can efficiently increase T_c in OsBr₂. Additionally, doping of a few electrons can significantly increase the PMAE of OsCl₂ whose intrinsic T_c is far beyond the room temperature. The results suggest OsCl₂ and OsBr₂ have a great potential for magnetic storage and valleytronic application in a wide temperature span.

ACKNOWLEDGMENTS

This paper was supported by National Natural Science Foundation of China (Grants No. 12174450 and No. 11874429), National High-level Talents Program, Distinguished Youth Foundation of Hunan Province (Grant No. 2020JJ2039), Project of High-Level Talents Accumulation of Hunan Province (Grant No. 2018RS3021), Hunan Provincial Key Research and Development Program (Grant No. 2022WK2002), and Program of Hundreds of Talents of Hunan Province, State Key Laboratory of Powder Metallurgy, Start-Up Funding and Innovation-Driven Plan (Grant No. 2019CX023) of Central South University. Calculations and simulations were performed at High-Performance Computing facilities of Central South University.

-
- [1] K. Ando, Seeking room-temperature ferromagnetic semiconductors, *Science* **312**, 1883 (2006).
 - [2] C. Huang, J. Feng, F. Wu, D. Ahmed, B. Huang, H. Xiang, K. Deng, and E. Kan, Toward intrinsic room-temperature ferromagnetism in two-dimensional semiconductors, *J. Am. Chem. Soc.* **140**, 11519 (2018).
 - [3] A. Rycerz, J. Tworzydło, and C. W. J. Beenakker, Valley filter and valley valve in graphene, *Nature Phys.* **3**, 172 (2007).
 - [4] J. R. Schaibley, H. Yu, G. Clark, P. Rivera, J. S. Ross, K. L. Seyler, W. Yao, and X. Xu, Valleytronics in 2D materials, *Nat. Rev. Mater.* **1**, 16055 (2016).
 - [5] L. L. Tao and E. Y. Tsymbal, Two-dimensional spin-valley locking spin valve, *Phys. Rev. B* **100**, 161110(R) (2019).
 - [6] W. Y. Tong, S. J. Gong, X. Wan, and C. G. Duan, Concepts of ferrovalley material and anomalous valley Hall effect, *Nat. Commun.* **7**, 13612 (2016).
 - [7] J. W. Chu, Y. Wang, X. P. Wang, K. Hu, G. F. Rao, C. H. Gong, C. C. Wu, H. Hong, X. F. Wang, K. H. Liu *et al.*, 2D polarized materials: Ferromagnetic, ferrovalley, ferroelectric materials, and related heterostructures, *Adv. Mater.* **33**, 2004469 (2021).

- [8] X. Xu, W. Yao, D. Xiao, and T. F. Heinz, Spin and pseudospins in layered transition metal dichalcogenides, *Nature Phys.* **10**, 343 (2014).
- [9] P. Zhao, Y. Ma, C. Lei, H. Wang, B. Huang, and Y. Dai, Single-layer LaBr₂: Two-dimensional valleytronic semiconductor with spontaneous spin and valley polarizations, *Appl. Phys. Lett.* **115**, 261605 (2019).
- [10] S. D. Guo, J. X. Zhu, W. Q. Mu, and B. G. Liu, Possible way to achieve anomalous valley Hall effect by piezoelectric effect in a GdCl₂ monolayer, *Phys. Rev. B* **104**, 224428 (2021).
- [11] R. Li, J. Jiang, W. Mi, and H. Bai, Room temperature spontaneous valley polarization in two-dimensional FeClBr monolayer, *Nanoscale* **13**, 14807 (2021).
- [12] K. Sheng, B. Zhang, H. K. Yuan, and Z. Y. Wang, Strain-engineered topological phase transitions in ferrovalley 2H-RuCl₂ monolayer, *Phys. Rev. B* **105**, 195312 (2022).
- [13] H. Zheng, H. Han, J. Zheng, and Y. Yan, Strain tuned magnetocrystalline anisotropy in ferromagnetic H-FeCl₂ monolayer, *Solid State Commun.* **271**, 66 (2018).
- [14] Y. Ma, Y. Wu, J. Tong, L. Deng, X. Yin, L. Zhou, X. Han, F. Tian, and X. Zhang, Distinct ferrovalley characteristics of the Janus RuClX (X = F, Br) monolayer, *Nanoscale* **15**, 8278 (2023).
- [15] H. X. Cheng, J. Zhou, W. Ji, Y. N. Zhang, and Y. P. Feng, Two-dimensional intrinsic ferrovalley GdI₂ with large valley polarization, *Phys. Rev. B* **103**, 125121 (2021).
- [16] S. D. Guo, J. X. Zhu, M. Y. Yin, and B. G. Liu, Substantial electronic correlation effects on the electronic properties in a Janus FeClF monolayer, *Phys. Rev. B* **105**, 104416 (2022).
- [17] P. Zhao, Y. Dai, H. Wang, B. Huang, and Y. Ma, Intrinsic valley polarization and anomalous valley Hall effect in single-layer 2H-FeCl₂, *ChemPhysMater* **1**, 56 (2022).
- [18] W. Pan, Tuning the magnetic anisotropy and topological phase with electronic correlation in single-layer H-FeBr₂, *Phys. Rev. B* **106**, 125122 (2022).
- [19] H. Sun, S. S. Li, W. X. Ji, and C. W. Zhang, Valley-dependent topological phase transition and quantum anomalous valley Hall effect in single-layer RuClBr, *Phys. Rev. B* **105**, 195112 (2022).
- [20] H. Huan, Y. Xue, B. Zhao, G. Gao, H. Bao, and Z. Yang, Strain-induced half-valley metals and topological phase transitions in MBr₂ monolayers (M = Ru, Os), *Phys. Rev. B* **104**, 165427 (2021).
- [21] R. Li, N. Mao, X. Wu, B. Huang, Y. Dai, and C. Niu, Robust second-order topological insulators with giant valley polarization in two-dimensional honeycomb ferromagnets, *Nano Lett.* **23**, 91 (2023).
- [22] S. D. Guo, W. Q. Mu, and B. G. Liu, Valley-polarized quantum anomalous Hall insulator in monolayer RuBr₂, *2D Mater.* **9**, 035011 (2022).
- [23] S. D. Guo, Y. L. Tao, W. Q. Mu, and B. G. Liu, Correlation-driven threefold topological phase transition in monolayer OsBr₂, *Front. Phys.* **18**, 33304 (2023).
- [24] X. Kong, L. Li, L. Liang, F. M. Peeters, and X. J. Liu, The magnetic, electronic, and light-induced topological properties in two-dimensional hexagonal FeX₂ (X = Cl, Br, I) monolayers, *Appl. Phys. Lett.* **116**, 192404 (2020).
- [25] H. Hu, W. Y. Tong, Y. H. Shen, X. Wan, and C. G. Duan, Concepts of the half-valley-metal and quantum anomalous valley Hall effect, *Npj Comput. Mater.* **6**, 129 (2020).
- [26] L. Cai, R. Li, X. Wu, B. Huang, Y. Dai, and C. Niu, Second-order topological insulators and tunable topological phase transitions in honeycomb ferromagnets, *Phys. Rev. B* **107**, 245116 (2023).
- [27] D.-s. Wang, R. Wu, and A. J. Freeman, First-principles theory of surface magnetocrystalline anisotropy and the diatomic-pair model, *Phys. Rev. B* **47**, 14932 (1993).
- [28] X. Wang, R. Wu, D.-s. Wang, and A. J. Freeman, Torque method for the theoretical determination of magnetocrystalline anisotropy, *Phys. Rev. B* **54**, 61 (1996).
- [29] G. Schneider, R. P. Erickson, and H. J. F. Jansen, Calculation of the magnetocrystalline anisotropy energy using a torque method, *J. Appl. Phys.* **81**, 3869 (1997).
- [30] P. E. Blöchl, Projector augmented-wave method, *Phys. Rev. B* **50**, 17953 (1994).
- [31] G. Kresse and J. Furthmüller, Efficiency of *ab-initio* total energy calculations for metals and semiconductors using a plane-wave basis set, *Comput. Mater. Sci.* **6**, 15 (1996).
- [32] J. P. Perdew, K. Burke, and M. Ernzerhof, Generalized gradient approximation made simple, *Phys. Rev. Lett.* **77**, 3865 (1996).
- [33] See Supplemental Material at <http://link.aps.org/supplemental/10.1103/PhysRevB.109.024406> for a comparison of band structures between PBE+U and HSE06; energy differences between FM and AFM; representation of polar and azimuth angles; projection of spin along the z axis; derivation of valley polarization; Berry curvature and AVH conductivity; contribution of atomic orbitals to MAE; impact of carrier doping on the MAE and band structures; calculated MAE in terms of torque method; and magnetic exchange parameter and Curie temperature calculation.
- [34] M. Weinert, R. E. Watson, and J. W. Davenport, Total-energy differences and eigenvalue sums, *Phys. Rev. B* **32**, 2115 (1985).
- [35] G. H. O. Daalderop, P. J. Kelly, and M. F. H. Schuurmans, First-principles calculation of the magnetocrystalline anisotropy energy of iron, cobalt, and nickel, *Phys. Rev. B* **41**, 11919 (1990).
- [36] J. Hu and R. Wu, Control of the magnetism and magnetic anisotropy of a single-molecule magnet with an electric field, *Phys. Rev. Lett.* **110**, 097202 (2013).
- [37] J. Hu and R. Wu, Giant magnetic anisotropy of transition-metal dimers on defected graphene, *Nano Lett.* **14**, 1853 (2014).
- [38] A. Togo and I. Tanaka, First principles phonon calculations in materials science, *Scr. Mater.* **108**, 1 (2015).
- [39] N. Marzari, A. A. Mostofi, J. R. Yates, I. Souza, and D. Vanderbilt, Maximally localized Wannier functions: Theory and applications, *Rev. Mod. Phys.* **84**, 1419 (2012).
- [40] L. Liu, X. Ren, J. Xie, B. Cheng, W. Liu, T. An, H. Qin, and J. Hu, Magnetic switches via electric field in BN nanoribbons, *Appl. Surf. Sci.* **480**, 300 (2019).
- [41] L. Liu, S. Chen, Z. Lin, and X. Zhang, A symmetry-breaking phase in two-dimensional FeTe₂ with ferromagnetism above room temperature, *J. Phys. Chem. Lett.* **11**, 7893 (2020).
- [42] L. Webster and J. A. Yan, Strain-tunable magnetic anisotropy in monolayer CrCl₃, CrBr₃, and CrI₃, *Phys. Rev. B* **98**, 144411 (2018).
- [43] M. C. Jiang and G. Y. Guo, Large magneto-optical effect and magnetic anisotropy energy in two-dimensional metallic ferromagnet Fe₃GeTe₂, *Phys. Rev. B* **105**, 014437 (2022).
- [44] S. Ji, Y. Wang, R. Yao, C. Quan, J. Yang, and X. Li, Dimension-dependent magnetic anisotropy for tunable anomalous Hall

- effect in transition metal dichalcogenides, *Phys. Rev. B* **107**, 035438 (2023).
- [45] K. Kořmider, J. W. González, and J. Fernández-Rossier, Large spin splitting in the conduction band of transition metal dichalcogenide monolayers, *Phys. Rev. B* **88**, 245436 (2013).
- [46] G. Aivazian, Z. Gong, A. M. Jones, R. L. Chu, J. Yan, D. G. Mandrus, C. Zhang, D. Cobden, W. Yao, and X. Xu, Magnetic control of valley pseudospin in monolayer WSe₂, *Nature Phys.* **11**, 148 (2015).
- [47] D. MacNeill, C. Heikes, K. F. Mak, Z. Anderson, A. Kormányos, V. Zólyomi, J. Park, and D. C. Ralph, Breaking of valley degeneracy by magnetic field in monolayer MoSe₂, *Phys. Rev. Lett.* **114**, 037401 (2015).
- [48] H. Xiang, C. Lee, H. J. Koo, X. Gong, and M. H. Whangbo, Magnetic properties and energy-mapping analysis, *Dalton Trans.* **42**, 823 (2013).
- [49] W. Xie, Y. Song, and X. Zuo, Transverse Rashba effect and unconventional magnetocrystalline anisotropy in graphene-nanoribbon-based centrosymmetric antiferromagnet, *Carbon* **185**, 619 (2021).
- [50] G. B. Liu, W. Y. Shan, Y. Yao, W. Yao, and D. Xiao, Three-band tight-binding model for monolayers of group-VIB transition metal dichalcogenides, *Phys. Rev. B* **88**, 085433 (2013).
- [51] D. J. Thouless, M. Kohmoto, M. P. Nightingale, and M. den Nijs, Quantized Hall conductance in a two-dimensional periodic potential, *Phys. Rev. Lett.* **49**, 405 (1982).